

Lewis Acid–Base-Driven Anisotropic Crystal Growth of Pyrochlore $\text{Pb}_2\text{Ti}_2\text{O}_{5.4}\text{F}_{1.2}$ with Enhanced Visible-Light H_2 Evolution Activity

Gentoku Kido, Hiroto Ueki, Megumi Okazaki, Jun Kikkawa, Koji Kimoto, Ryosuke Nishikubo, Akinori Saeki, and Kazuhiko Maeda*



Cite This: *Chem. Mater.* 2026, 38, 1980–1990



Read Online

ACCESS |



Metrics & More

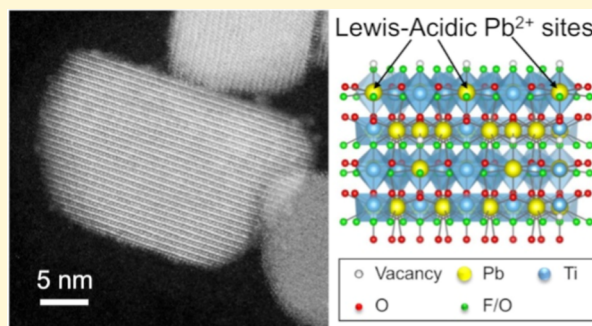


Article Recommendations



Supporting Information

ABSTRACT: Mixed-anion compounds offer unique functionalities unattainable with single-anion materials, yet rational morphology control remains largely unexplored. Here, we report a Lewis acid–base-driven strategy that enables low-temperature, solution-phase morphology control of the oxyfluoride photocatalyst $\text{Pb}_2\text{Ti}_2\text{O}_{5.4}\text{F}_{1.2}$ (PTOF). A microwave-assisted solvothermal method with monoethanolamine (MEA) was used to tune the particle morphology and size via the precursor-solution pH, which was adjusted by the addition of formic acid or acetic acid. PTOF, an $\text{A}_2\text{B}_2\text{X}_6\text{X}'_{0.5}$ -type pyrochlore with intrinsic anion vacancies (X'_2 , 4d site), has exposed {111} facets composed of alternating Pb-rich and Ti-rich layers. Lewis basic MEA is proposed to bind selectively to undercoordinated, strongly acidic Pb^{2+} sites adjacent to Ti^{4+} and vacancies on Ti-rich {111} facets, suppressing growth along the surface direction and stabilizing these facets, thereby driving anisotropic crystal growth and forming plate-like nanoparticles. At pH 10 (formic acid), PTOF nanoparticles (~ 30 nm) with a specific surface area of $37 \text{ m}^2 \text{ g}^{-1}$ were obtained. Compared with an analogous PTOF synthesized by a conventional solid–state reaction, the optimized sample exhibited ~ 29 -fold higher H_2 evolution activity in an aqueous solution containing dissolved disodium ethylenediaminetetraacetate under visible-light ($\lambda > 400 \text{ nm}$) with the aid of a Pt cocatalyst. Lewis acid–base-directed facet stabilization is thus shown to be a promising approach for the rational morphological design of mixed-anion oxyfluorides via solution processing.



INTRODUCTION

Controlled anisotropic crystal growth is a fundamental approach to tune structure–property relationships in materials chemistry. In heterogeneous photocatalysts, such control enables spatial separation of oxidation and reduction sites, thereby promoting directional charge transport and suppressing charge recombination.^{1–3} In oxide-based materials, such facet engineering has been demonstrated to dramatically enhance photocatalytic efficiency. For instance, Al-doped SrTiO_3 crystals with both {100} and {110} facets exposed have achieved apparent quantum yields (AQYs) approaching 100%, clearly indicating that particle morphology strongly governs charge separation and surface reactivity.¹ However, these advances have been limited almost exclusively to oxide systems. For visible-light-responsive mixed-anion photocatalysts—key materials for next-generation solar-to-fuel conversion—rational control of anisotropic crystal growth remains largely unexplored.

Mixed-anion compounds have emerged as promising photocatalysts because of their tunable electronic structures. The incorporation of less-electronegative anions such as N^{3-} , Cl^- , or S^{2-} into metal oxides raises the valence-band maximum, thereby narrowing the bandgap while maintaining

redox potentials suitable for water splitting.^{4–7} This feature enables the efficient utilization of visible light, overcoming the intrinsic trade-off in oxides, where bandgap narrowing typically makes the conduction band too positive for H_2 evolution.⁸ Despite these advantages, morphological control in mixed-anion systems remains scarcely developed because the synthesis involves multiple equilibria among competing anionic species. Differences in vapor pressure, anion exchange, or hydrolysis equilibria can easily induce compositional variations, making facet-selective growth highly challenging.

Nevertheless, researchers have achieved anisotropic crystal growth of several layered mixed-anion compounds such as BiOCl and $\text{Y}_2\text{Ti}_2\text{O}_5\text{S}_2$ by exploiting differences in anion size and charge.^{9–11} These systems naturally form alternating oxide and halide (or chalcogenide) layers, resulting in sheet-like morphologies with facet-dependent reactivity. By contrast,

Received: November 22, 2025

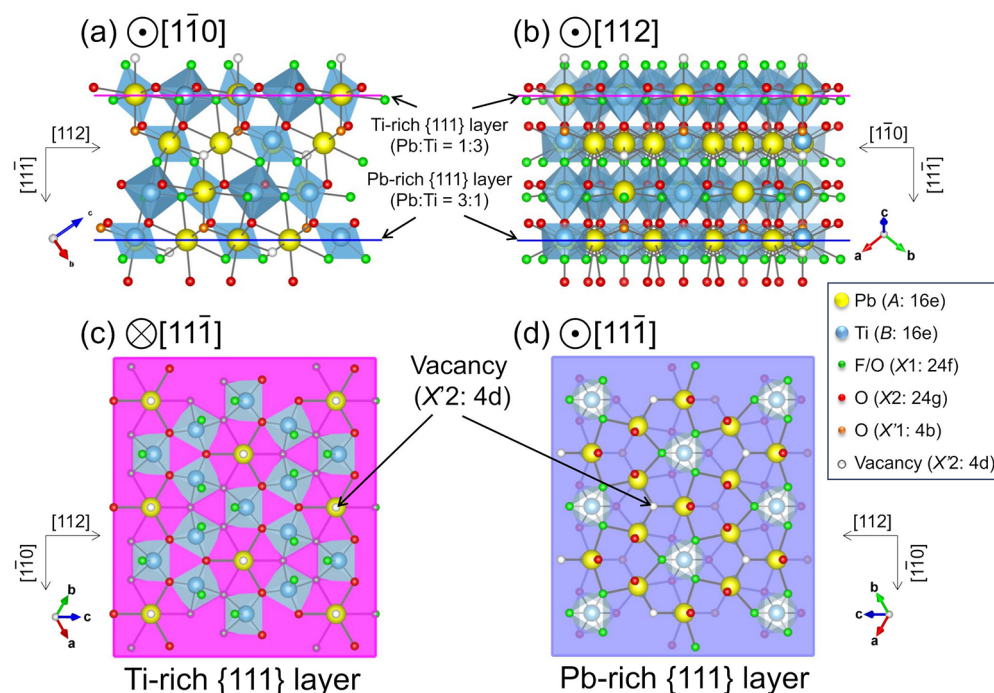
Revised: January 21, 2026

Accepted: January 23, 2026

Published: February 6, 2026



Scheme 1. Crystal Structure of $\text{Pb}_2\text{Ti}_2\text{O}_{5.4}\text{F}_{1.2}$ ($\text{A}_2\text{B}_2\text{X}_6\text{X}'_{0.5}$ -type Pyrochlore, Space Group $F\bar{4}3m$) Highlighting the $\{111\}$ Layer Stacking and Surface Terminations^a



^aIn this space group, the X and X' sites are divided into two nonequivalent positions, denoted as X1/X2 and X'1/X'2, respectively. (a) Crystal structure viewed along the $[1\bar{1}0]$ direction, showing the stacking of alternating Pb-rich and Ti-rich layers parallel to the $\{111\}$ planes. (b) Crystal structure viewed along the $[112]$ direction. (c) A Ti-rich $\{111\}$ facet viewed from the top of (a). (d) A Pb-rich $\{111\}$ facet viewed from the bottom of (a).

cubic oxyfluorides and oxynitrides—with minimal anion size mismatch—can tolerate extensive anion substitution without substantial lattice distortion. Although this structural flexibility enhances stability, it also stabilizes isotropic morphologies, making anisotropic growth far more difficult to achieve.^{12,13} Inducing anisotropic shapes in such cubic systems therefore requires subtle control over surface coordination and growth kinetics.^{14,15}

Among visible-light-responsive oxyfluorides, pyrochlore-type $\text{Pb}_2\text{Ti}_2\text{O}_{5.4}\text{F}_{1.2}$ (PTOF) represents a rare example that combines strong photochemical robustness with suitable band positions for visible-light water splitting. The hybridization between the Pb 6s² lone pair and O 2p orbitals, known as the “revised lone-pair” (RLP) effect, raises the valence-band energy and enables visible-light absorption, while F[−] ions further stabilize the framework by shortening Pb–O bonds.^{16–18} Unlike oxynitrides, which often suffer from self-oxidation due to high-energy N 2p-derived valence bands, PTOF maintains both high stability toward oxidation reactions and high structural integrity.^{16,19} However, conventional solid-state reactions (SSRs) yield coarse, featureless PTOF particles,¹⁶ and microwave-assisted hydrothermal methods typically produce isotropic octahedral crystals with multiple exposed facets.^{20,21} Developing a morphology control strategy for PTOF is thus critical to realizing its full potential as a model oxyfluoride photocatalyst.

Here, we introduce a Lewis acid–base coordination approach to direct anisotropic crystal growth of PTOF under microwave-assisted solvothermal (MST) conditions. Our motivation is not merely to tailor the morphology of a specific compound, but to demonstrate that chemically selective

interactions during solution-based synthesis can induce anisotropic growth even in crystallographically isotropic frameworks such as cubic pyrochlores. Inspired by recent studies on BiVO_4 and TaO_2F , where soft Lewis bases such as monoethanolamine (MEA) selectively coordinate to cationic sites and stabilize specific facets,^{22,23} we extend this concept to a visible-light-active, mixed-anion oxyfluoride system for the first time. As shown in Scheme 1a,b, PTOF, a $\text{A}_2\text{B}_2\text{X}_6\text{X}'_{0.5}$ -type pyrochlore with space group $F\bar{4}3m$, consists of alternating Pb²⁺-rich and Ti⁴⁺-rich layers stacking along the $\langle 111 \rangle$ direction. In this space group, the X and X' sites are divided into two nonequivalent positions, denoted as X1/X2 and X'1/X'2, respectively. Anion vacancies at the X'2 (4d) sites induce Lewis acidity at adjacent Pb²⁺ centers; this effect is stronger in Ti-rich $\{111\}$ layers, where the vacancy is localized around a single Pb²⁺ ion and the surrounding Ti⁴⁺ ions exert an electron-withdrawing influence (Scheme 1c,d). Therefore, Lewis basic MEA molecules are likely to coordinate to these under-coordinated Pb²⁺ centers associated with the intrinsic X'2 vacancy,^{16,18} thereby stabilizing Pb-rich facets and promoting anisotropic growth. To facilitate oxide network formation under solvothermal conditions, we used a liquid-phase deposition (LPD) reaction between $[\text{TiF}_6]^{2-}$ and boric acid, where boric acid irreversibly scavenges F[−] as BF_4^- , driving hydrolysis and the condensation of Ti–O bonds.²⁴ Microwave heating (2.45 GHz) ensures rapid and homogeneous thermal distribution, enabling precise control of nucleation and growth kinetics.

We systematically investigated the influence of precursor composition and pH on the physicochemical properties of the resultant PTOF samples using various analytical tools. The

correlation between anisotropic morphology and photocatalytic H₂ evolution activity under visible light reveals how Lewis base-driven facet stabilization governs crystal growth in cubic mixed-anion frameworks. This study thus provides mechanistic insight into how chemically selective coordination can break apparent crystallographic isotropy during growth, and offers a general design strategy for morphology-controlled oxyfluoride semiconductors, potentially extendable to other pyrochlore-type and related mixed-anion materials.

EXPERIMENTAL SECTION

Materials

(NH₄)₂TiF₆ (Thermo Fisher Scientific, 99.99%), Pb(CH₃COO)₂·3H₂O (Kanto Chemical, ≥99.5%), H₃BO₃ (Kanto Chemical, ≥99.5%), monoethanolamine (MEA; Kanto Chemical, ≥99.0%), formic acid (Kanto Chemical, ≥98%), acetic acid (Kanto Chemical, ≥99.7%), nitric acid (Kanto Chemical, EL grade), ethanol (Kanto Chemical, ≥99.5%), H₂PtCl₆·6H₂O (Mitsuiwa Chemical, 38% as Pt), and ethylenediaminetetraacetic acid disodium salt (EDTA·2Na; Dojindo Molecular Technologies, ≥99.5%) were used as received without further purification. A Ti standard solution (1000 mg L⁻¹, Kanto Chemical, for atomic absorption spectrometry), a Pb standard solution (1000 mg L⁻¹, Kanto Chemical, Japan Calibration Service System (JCSS) certified for chemical analysis), and an F⁻ standard solution (1000 mg L⁻¹, Kanto Chemical, JCSS certified for chemical analysis) were used as supplied.

Synthesis of Photocatalysts

PTOF samples were synthesized using the MST method with MEA as the solvent. A precursor solution was prepared by mixing 20 mL of 0.25 M (NH₄)₂TiF₆ MEA solution (5 mmol), 10 mL of 0.55 M Pb(CH₃COO)₂·3H₂O MEA solution (5.5 mmol), and 10 mL of 1.0 M H₃BO₃ MEA solution (10 mmol) in a Teflon vessel. The initial pH of the solution ranged from approximately 12.0 to 12.3. The pH was adjusted to 8 or 10 using formic acid or acetic acid. Because neutralization is exothermic, the pH adjustment was carried out in an ice bath to maintain the solution temperature at 323 K. When the addition of acid increased the total solution volume, the total volume of the solution was limited to ≤50% of the reaction-vessel capacity.

The Teflon vessel containing the precursor solution was then placed in a ceramic pressure jacket and heated by microwaves at 473 K for 2 h, followed by natural cooling. The internal pressure of the vessel reached 6 MPa under all conditions. The product was filtered and washed sequentially with MEA, ethanol, 0.1 M HNO₃ aqueous solution, and distilled water. Finally, it was vacuum-dried at 383 K. The product was named “MST-pHX(Y)” on the basis of the initial pH (X = 8, 10, 12) and the acid used for pH adjustment (Y = “none,” “FA” for formic acid, or “AA” for acetic acid). The entire materials preparation procedure is depicted in Scheme 2.

Characterization

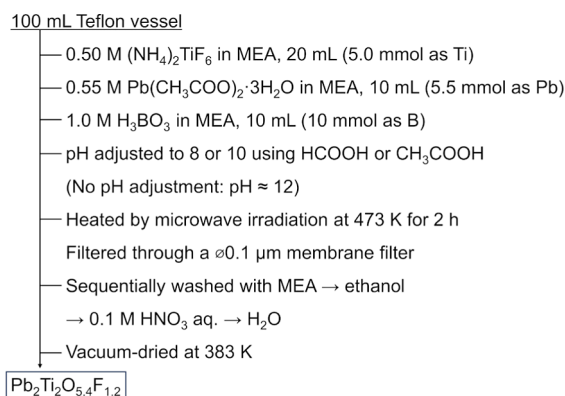
Powder XRD patterns were collected on a Rigaku SmartLab diffractometer equipped with a Cu Kα radiation source (λ = 1.5418 Å). The Scherrer equation was used to calculate the crystallite size on the basis of the peak broadening²⁵

$$D = \frac{K\lambda}{\beta \cos \theta}$$

where *D* represents the crystallite size (nm), *K* is the Scherrer constant, λ is the wavelength of the X-rays (nm), β is the peak broadening (rad), and θ is the Bragg angle (rad). The full-width at half-maximum was used for measurement of the peak broadening, and a Scherrer constant of 0.94 was applied. To check if the sample showed a preferred orientation, we calculated the Lotgering factor (*F*), which is defined by the following equation²⁶

$$F = \frac{P - P_0}{1 - P_0}$$

Scheme 2. Procedure for the Synthesis of Pb₂Ti₂O_{5.4}F_{1.2} via a Microwave-Assisted Solvothermal (MST) Method



where *P* is the ratio of the total intensity of selected peaks (in the range 10° ≤ 2θ ≤ 60°) to the total intensity of all peaks in the XRD pattern for the sample and *P*₀ is the same ratio for a randomly oriented sample.

$$P = \frac{\sum I(hkl)_{\text{selected}}}{\sum I(hkl)_{\text{total}}}, \quad P_0 = \frac{\sum I_0(hkl)_{\text{selected}}}{\sum I_0(hkl)_{\text{total}}}$$

All intensities were corrected by background subtraction using the FullProf software.²⁷ A higher Lotgering factor (closer to 1) indicates a stronger preferred orientation along the selected planes. Rietveld refinement of the powder XRD patterns was performed using the RIETAN-FP program.²⁸ A reported structural model of PTOF was employed as the initial model,¹⁸ and only the lattice parameters were refined, while all atomic positions, occupancies, and atomic displacement parameters were fixed. Peak shapes were modeled using a pseudo-Voigt function, and the background was fitted with a polynomial function. The refined lattice parameters were used only for qualitative comparison among samples, and no further structural parameters were extracted from the refinement.

SEM images were obtained using a Hitachi High-Tech Regulus 8230 field-emission scanning electron microscope. Specific surface areas and pore-size distributions were measured by N₂ adsorption-desorption at 77 K using a BELSORP-mini X analyzer and were calculated via the Brunauer–Emmett–Teller (BET) and Barrett–Joyner–Halenda (BJH) methods, respectively. UV–vis diffuse-reflectance spectra were recorded on a JASCO V-770 spectrophotometer equipped with an integrating sphere. Bulk elemental compositions were analyzed by inductively coupled plasma optical emission spectroscopy (ICP-OES, Agilent 720) and combustion ion chromatography (Nittoseiko Analytech). Surface compositions were examined by X-ray photoelectron spectroscopy (XPS, ULVAC-PHI PHI5000 VersaProbe III). Flat-band potentials were determined from Mott–Schottky plots acquired at 100 Hz using a HZ-Pro potentiostat and 0.1 M sodium phosphate buffer solution at pH 3.0, 6.6, or 11.9. Scanning transmission electron microscopy (STEM) images were acquired using an electron microscope (FEI Titan Cubed) equipped with spherical aberration correctors (CEOS) and operated at an acceleration voltage of 300 kV with a probe current of approximately 20 pA. Observations using STEM with energy-dispersive X-ray spectroscopy (STEM-EDS) were conducted under nearly identical conditions using a Themis Z transmission electron microscope (Thermo Fisher Scientific) operated at 300 kV with a probe current of approximately 200 pA. Time-resolved microwave conductivity (TRMC) measurements were carried out using a 9.1 GHz X-band microwave cavity system to evaluate the photogenerated charge-carrier dynamics under pulsed laser excitation (355 nm). Powder samples were fixed on a quartz substrate using adhesive tape and were photoexcited by a Nd:YAG laser (Continuum, Surelite II; pulse width: 5–8 ns; repetition rate: 10 Hz) at an incident photon density of *I*₀ = 9.1 × 10¹⁵ photons cm⁻² pulse⁻¹. The photoconductivity (Δσ

$= \Delta P_r / (AP_r)$, where A is the sensitivity factor, P_r is the reflected microwave power, and ΔP_r is its change upon photoirradiation) was converted to the product of the quantum yield (φ) and the sum of the charge-carrier mobilities ($\Sigma\mu = \mu^+ + \mu^-$) according to the equation $\varphi\Sigma\mu = \Delta\sigma(eI_0F_{\text{light}})^{-1}$, where e is the elementary charge and F_{light} is a correction (or filling) factor. The TRMC measurements were carried out in air at room temperature.

Photocatalytic Test

Photocatalytic H_2 evolution reactions were performed in a closed gas-circulation reactor connected to a gas chromatograph (Shimadzu GC-2014s). The reaction suspension consisted of 100 mg PTOF photocatalyst dispersed in 140 mL of aqueous solution containing 10 mM EDTA-2Na as a sacrificial reagent. Pt (0.5 wt %) was photodeposited in situ as a cocatalyst using a 300 W Xe lamp (Cermex PE300BF) equipped with an L42 cutoff filter ($\lambda > 400$ nm). The reaction mixture was maintained at 290 K by a cooling-water circulation system. H_2 evolution was monitored periodically by gas chromatography.

For AQY measurements, irradiation with monochromatic light was carried out using a MAX-303 Xe lamp equipped with 365, 400, 420, and 460 nm bandpass filters (bandwidth: ± 10 nm). The photon flux at each wavelength was determined using a calibrated spectroradiometer (LS-100, Eko Instruments). The AQY was calculated according to the equation

$$\text{AQY (\%)} = \frac{A \times R}{I} \times 100$$

where A is the reaction coefficient, R is the rate of H_2 evolution (mol s^{-1}), and I is the number of incident photons per second. In the presence of EDTA as an electron donor, a current-doubling effect is assumed, meaning that one photon effectively leads to one molecule of H_2 ($A = 1$).⁵⁹ The photon intensity at each wavelength was measured using a spectroradiometer (LS-100, Eko Instruments).

RESULTS AND DISCUSSION

Material Characterization

Figure 1 shows XRD patterns for PTOF synthesized by the MST method (initial pH 8–12) and the SSR method. All

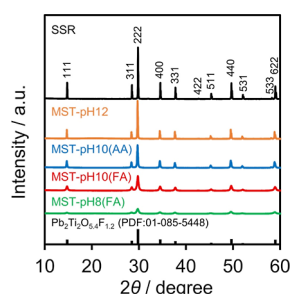


Figure 1. XRD patterns for $\text{Pb}_2\text{Ti}_2\text{O}_{5.4}\text{F}_{1.2}$ synthesized by the MST method under different pH conditions and by SSR. Parenthetical abbreviations indicate the acid used for pH adjustment: AA = acetic acid, FA = formic acid.

diffraction peaks matched well with those of the reference pattern (PDF #01-085-5448), confirming the formation of phase-pure PTOF. Notably, in the absence of boric acid, PTOF was not obtained as the primary phase (Figure S1), indicating that the boric acid-induced liquid-phase deposition (LPD) reaction—where F^- ions are irreversibly captured as BF_4^- ions—is the principal formation mechanism in this system.

In the MST samples, decreasing the initial pH toward neutral (pH 8–10) resulted in pronounced peak broadening, reflecting a reduced crystallite size. This trend is attributed to

partial neutralization of MEA upon acid addition, leading to carbamate formation and the weakening of MEA-Pb^{2+} interactions, which in turn promotes homogeneous nucleation in solution. In particular, the use of formic acid instead of acetic acid led to a more pronounced reduction in particle size (Figures 1 and S2). This decrease in particle size is likely attributable to formic acid decomposing readily at the reaction temperature (~ 380 K) and the resulting H_2O slightly shifting the pH toward basic conditions, accelerating hydrolysis, increasing supersaturation, and thereby enhancing the nucleation rate.

The bulk and surface compositions of the samples are summarized in Table 1. For all of the samples, the bulk composition ranges were $0.8 \leq \text{Pb/Ti} \leq 1.0$ and $0.6 \leq \text{F/Ti} \leq 0.8$, which are close to the ideal stoichiometry of $\text{Pb}_2\text{Ti}_2\text{O}_{5.4}\text{F}_{1.2}$ ($\text{Pb/Ti} = 1$, $\text{F/Ti} = 0.6$). However, as the initial pH was decreased from 12 to 8, the Pb content gradually decreased and the F content increased. A similar trend was observed in the surface composition determined by XPS analysis (Figure S3). This pH dependence can be interpreted as resulting from the suppression of hydrolysis reactions under near-neutral conditions, which are otherwise favored at high pH, thereby allowing relatively greater incorporation of F^- ions.

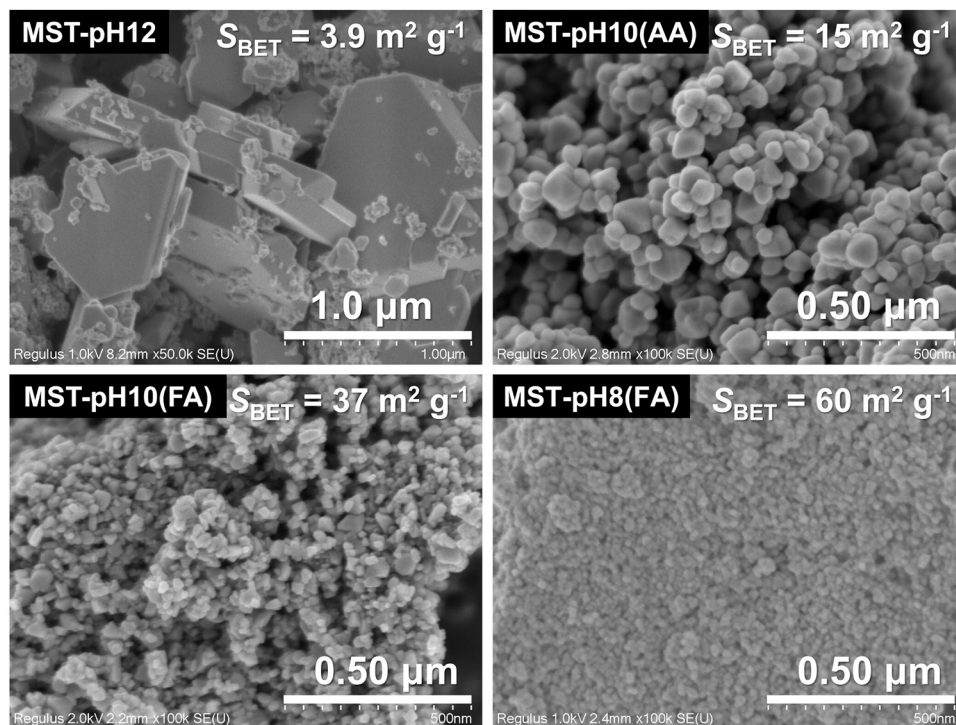
To assess whether the compositional variations observed among the MST-derived samples are manifested in their average crystal structures, lattice parameters were evaluated by Rietveld refinement of the XRD patterns using a reported structural model of PTOF.¹⁸ In this analysis, only the lattice parameters were refined, while all other structural parameters were fixed (Figure S4). Within the MST series, a slight lattice contraction was observed for the samples synthesized under near-neutral conditions, namely MST-pH10(FA) and MST-pH8(FA), which qualitatively correlates with the reduced Pb content listed in Table 1. By contrast, the lattice parameters of the MST-derived samples were generally slightly larger than those of the SSR-derived sample. This discrepancy cannot be readily attributed solely to differences in synthesis temperature or bulk composition, and instead likely reflects local structural distortions and/or short-range disorder introduced by the low-temperature solution-based synthesis, effects that are not fully captured by the average crystal structure.

Analysis of the MST-pH10(FA) sample by thermogravimetry–mass spectrometry (TG–MS) (Figure S5) revealed mass losses of approximately 1.2% at ~ 550 K and 0.7% at ~ 850 K. Mass spectrometric analysis of the evolved gas detected signals at $m/z = 18$, 30, and 44, which are assigned to H_2O , HCHO , and CO_2 , respectively. Although the exact contribution of water is uncertain, the total organic residue content was estimated to be at most ~ 2 wt.%.

SEM observations (Figure 2) revealed that the MST-derived samples exhibited distinct morphologies depending on the initial pH conditions. For the samples prepared under pH 12, micron-sized hexagonal plate-like particles were observed; however, their morphologies differed depending on the acid used to adjust the pH. For the sample prepared under pH 10 using acetic acid, truncated octahedral particles with sizes of 50–100 nm were formed; by contrast, plate-like particles with sizes of 30–50 nm were obtained in the sample prepared at pH 10 using formic acid. A further size reduction to less than 30 nm was achieved at pH 8 (formic acid), yielding a specific surface area of $60 \text{ m}^2 \text{ g}^{-1}$, the largest specific surface area ever reported for PTOF. By contrast, the SSR sample consisted of

Table 1. Bulk and Surface Atomic Ratios for $\text{Pb}_2\text{Ti}_2\text{O}_{5.4}\text{F}_{1.2}$ Synthesized by the MST Method under Different pH Conditions and by SSR

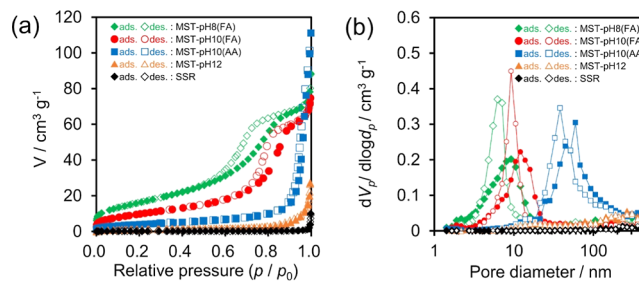
sample	bulk atomic ratio ^a		surface atomic ratio ^b		
	Pb/Ti	F/Ti	Pb/Ti	F/Ti	O/Ti
ideal	1.0	0.60	1.0	0.60	2.7
MST-pH8(FA)	0.83 ± 0.008	0.78 ± 0.01	1.0	0.89	2.6
MST-pH10(FA)	0.89 ± 0.006	0.57 ± 0.01	1.0	0.50	2.9
MST-pH10(AA)	0.94 ± 0.008	0.66 ± 0.01	1.1	0.67	2.7
MST-pH12	0.95 ± 0.015	0.65 ± 0.008	1.5	0.68	3.2
SSR	1.0 ± 0.04	0.47 ± 0.01	1.8	0.72	8.4

^aMeasured by ICP-OES, and F was measured by combustion ion chromatography. The standard deviation of three measurements is listed.^bCalculated from the corresponding XPS peak areas (Figure S3).**Figure 2.** SEM images of PTOF synthesized by the MST method under various pH conditions.

coarse particles several micrometers in size, with a markedly lower specific surface area of $0.43 \text{ m}^2 \text{ g}^{-1}$.

The Lotgering orientation factors, which were calculated from the XRD peak intensity ratios (Table S1), were within ± 0.1 for all of the samples, indicating that the samples can be classified as weakly oriented. Therefore, simple flat pressing of the powder during sample preparation did not induce substantial texturing. Nevertheless, in the XRD pattern for the MST-pH12 sample, the 222 reflection was slightly enhanced, suggesting that the broad surfaces of the plate-like particles observed in SEM correspond to the $\{111\}$ planes. The wide facets observed in the SEM images appear consistent with $\{111\}$, whereas the side facets may correspond to other low- to intermediate-index planes. However, this assignment remains tentative and is based solely on morphological observation.

Figure 3a shows N_2 adsorption–desorption isotherms for PTOF samples synthesized by the MST method under different initial pH conditions, as well as those for samples synthesized by SSR. The isotherms for the samples prepared at pH 8 and 10 (formic acid) are type IV, indicating the presence

**Figure 3.** (a) N_2 adsorption–desorption isotherms for $\text{Pb}_2\text{Ti}_2\text{O}_{5.4}\text{F}_{1.2}$ synthesized by the MST method under different pH conditions and by SSR. (b) Corresponding BJH pore-size distributions.

of mesopores. The pore size distributions calculated by the BJH method (Figure 3b) show peaks in the region below 10 nm for MST-pH8(FA), in the region around 10 nm for MST-pH10(FA), and in the 50–100 nm region for MST-pH10(AA), which correspond well to the interparticle voids observed in the SEM images (Figure 2).

The apparent density estimated from the regression line in Figure S6 (6.3 g cm^{-3}) was reasonably close to the theoretical

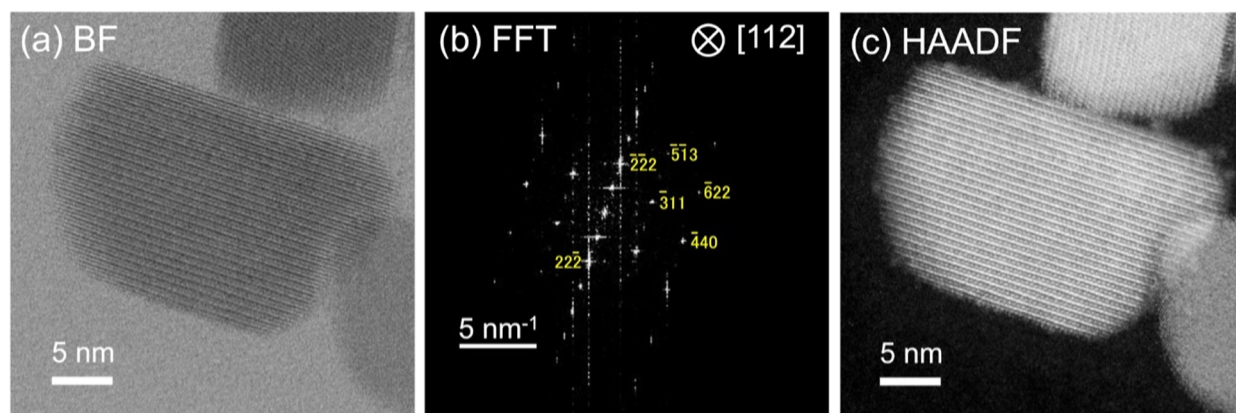


Figure 4. (a) Bright-field (BF) STEM image of the MST-pH10(FA) PTOF sample. (b) Fast Fourier transform (FFT) pattern obtained from the particle shown in panel (a). This image represents the reciprocal-space information. (c) High-angle annular dark-field (HAADF) STEM image of the same sample.

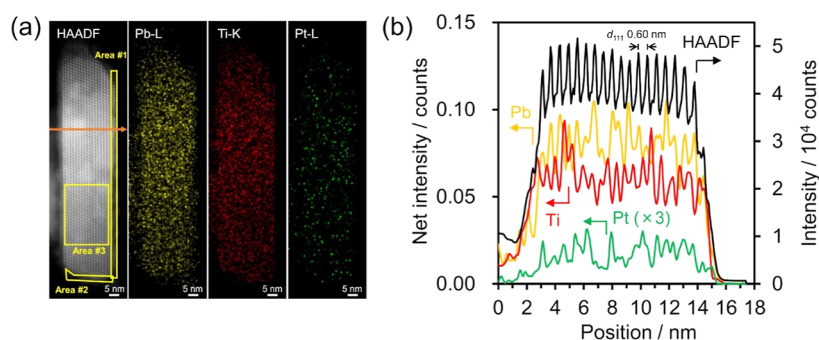


Figure 5. (a) HAADF-STEM image of MST-pH10-FA with overlaid EDS maps of Pb, Ti, and Pt. (b) Line mapping along the direction indicated by the orange arrow in panel (a). The Pt signal is magnified 5-fold for clarity. The sample was prepared by in situ photodeposition of Pt, followed by a photocatalytic reaction conducted for 10 h. The Pt loading amount was quantified by ICP-OES to be 0.4 wt %.

density calculated from the crystal structure (7.36 g cm^{-3}). This agreement suggests that, in the high-surface-area samples, the crystallites predominantly exist as discrete, single-crystalline nanoparticles, with minor contributions from surface roughness or interparticle voids. The estimation assumed nonaggregated, spherical particles, which is a widely accepted approach for nonporous materials when a linear relationship is observed between S_{BET} and $1/D$.³⁰ By contrast, the slopes for samples with lower specific surface areas deviated from that predicted by the theoretical density, indicating the formation of aggregated or polycrystalline particles, consistent with results of previous reports in which this method was applied to oxide systems.³¹

Notably, the crystallite sizes estimated by the Scherrer equation for MST-pH10(FA), MST-pH8(FA), and MST-pH10(AA) were consistent with the particle sizes observed by SEM and the peak pore diameters from the BJH analysis (Table S2), supporting the assumption that these samples consist of single-crystalline nanoparticles. Overall, the MST-derived samples exhibited mesoporosity ($\leq 50 \text{ nm}$), with MST-pH8(FA) and MST-pH10(FA) particularly enriched in sub-10 nm mesopores.

To directly confirm these structural assignments, we carried out STEM and EDS analyses. As shown in Figure S7, repeated EDS frame accumulation led to gradual sample decomposition and the formation of Pb nanoparticles on the surface. Therefore, special care must be taken regarding the electron beam conditions, particularly the beam current. Similar beam-induced damage has been reported for PTOF in previous

studies.²¹ Figure 4a shows a bright-field (BF) STEM image of MST-pH10(FA). The particles were approximately 20 nm in size and exhibited single-crystalline characteristics, consistent with the XRD, SEM, and BJH results. For Grain A, whose zone axis was aligned, the fast Fourier transform (FFT) pattern (Figure 4b) confirmed observation along the $[112]$ direction. The corresponding high-angle annular dark-field (HAADF) STEM image is shown in Figure 4c. Because the HAADF intensity approximately scales with the square of the atomic number Z , Pb ($Z = 82$) appears brighter than Ti ($Z = 22$), whereas O ($Z = 8$) and F ($Z = 9$) are barely visible. The observed bright-spot arrangement matched the alternating stacking of Pb-rich layers (Pb/Ti = 3:1) and Ti-rich layers (Pb/Ti = 1:3) along the $\langle 111 \rangle$ direction, as expected from the crystal structure of $\text{Pb}_2\text{Ti}_2\text{O}_{5.4}\text{F}_{1.2}$. Figure 4 suggests that the $\{112\}$ facets are exposed, corresponding to Scheme 1b, whereas Figure S8 indicates that not only the $\{112\}$ but also the $\{110\}$ facets may be exposed, although a slight deviation of the zone axis prevented definitive identification. These results imply that, in the MST-pH10(FA) sample, the top and bottom surfaces correspond to the $\{111\}$ facets, whereas the side surfaces may involve the exposure of both $\{112\}$ and $\{110\}$ facets. In the Ti-rich layers, the lower Pb occupancy makes individual Pb atomic columns appear more pronounced in the HAADF image, whereas in the Pb-rich layers, the higher Pb content gives rise to densely arranged bright columns. This observation provides strong evidence that MEA selectively modifies the $\{111\}$ facets, promoting anisotropic crystal growth. Interestingly, termination along the $\langle 111 \rangle$ stacking

direction was observed as a Ti-rich layer with lower brightness compared with Pb, which suggests that MEA is preferentially adsorbed onto Ti-rich {111} facets where Pb^{2+} centers possess stronger Lewis acidity because of nearby Ti^{4+} and anion vacancies.

A direct control experiment without MEA was not feasible in this system. When MEA was excluded from the MST synthesis, a homogeneous precursor solution could not be obtained under otherwise identical conditions using either common protic polar solvents (e.g., water and ethylene glycol) or nonprotic polar solvents (e.g., 1-methyl-2-pyrrolidone and *N,N*-dimethylformamide), because the starting materials ($(\text{NH}_4)_2\text{TiF}_6$, $\text{Pb}(\text{CH}_3\text{COO})_2 \cdot 3\text{H}_2\text{O}$, and H_3BO_3) could not be simultaneously dissolved. Although dimethyl sulfoxide was able to dissolve all precursors, subsequent heating led to solvent decomposition and the formation of rutile-type oxide phases rather than PTOF. These results demonstrate that MEA does not function merely as a solvent, but plays an essential chemical role in stabilizing the precursor species and enabling the formation of the PTOF phase. Consequently, the anisotropic crystal growth behavior discussed above cannot be realized in the absence of MEA.

Before considering the photocatalytic performance, we first discuss the microstructure and surface composition of the Pt-loaded MST-pH10(FA) sample, which were examined by HAADF-STEM and EDS analyses, respectively. Figure 5a shows a HAADF-STEM image together with the corresponding elemental maps of Pb, Ti, and Pt, and Figure 5b presents an EDS line profile obtained along the orange arrow indicated in Figure 5a. Semiquantitative elemental ratios for the regions marked as Area #1 (assigned to a {111} facet), Area #2 (presumably a {110}–{112} facet), and Area #3 (bulk) are summarized in Table 2. The surface regions (Areas #1 and #2),

Table 2. Elemental Compositions of Pt-Loaded PTOF^a

element	mass fraction (%)			
	ideal	area #1	area #2	area #3
¹⁶ O–K	13.9	16(1)	16(4)	14(1)
¹⁹ F–K	3.6	1.6(5)	2(2)	4.4(9)
⁴⁸ Ti–K	15.4	22(3)	27(6)	18(3)
⁷⁸ Pt–L	0.5	3(1)	4(7)	1.7(3)
²⁰⁸ Pb–L	66.6	57(4)	50(7)	62(3)

^aMeasured by EDS for the selected areas (#1–#3) in the HAADF-STEM image (Figure 5a).

corresponding to only a few atomic layers, contained less Pb and F than the bulk region (Area #3), indicating a Ti-rich, oxide-like composition. This surface composition likely originates from the partial hydrolysis of Ti species during MST synthesis. The formic acid used for pH adjustment can thermally decompose to generate water, which promotes hydrolysis and suppresses further crystal growth. In the early stage of nucleation, the selective coordination of MEA to undercoordinated Pb^{2+} centers directed the formation of Ti-rich {111} facets, whereas subsequent hydrolysis of Ti species suppressed further crystal growth, resulting in nanosized particles with exposed Ti-terminated surfaces.

Because this sample was used as the Pt-loaded photocatalyst in the subsequent photocatalytic experiments, the distribution of Pt was investigated as well. No distinct Pt nanoparticles

were observed; instead, Pt appeared to be atomically dispersed across the entire particle surface.

Photophysical Properties and Band-Edge Potentials

According to the UV–vis diffuse reflectance spectra (Figure 6), the PTOF samples synthesized by the MST method exhibited

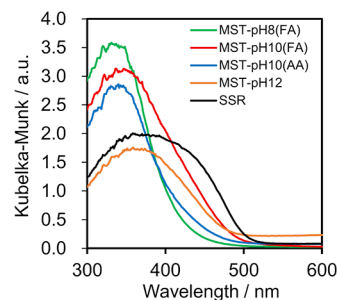


Figure 6. DRS of $\text{Pb}_2\text{Ti}_2\text{O}_{5.4}\text{F}_{1.2}$ synthesized by the MST method under different pH conditions and by SSR.

a noticeable blue shift in the absorption edge compared with the SSR-derived sample. This shift was more pronounced in samples synthesized under pH conditions closer to neutral. Mott–Schottky measurements (Figure 7) indicated that the conduction band edge remained largely unchanged among the samples, suggesting that the absorption edge shift is primarily attributable to a lowering of the valence-band maximum. This shift is likely due to Pb deficiency (as demonstrated by ICP-OES, Table 1), which weakens the hybridization between the Pb 6s and O 2p orbitals,¹⁷ thereby lowering the energy position of the valence band.

Figure 8a,b show time-dependent TRMC signals, revealing differences in the maximum photoconductivity ($\varphi\Sigma\mu_{\text{max}}$) and carrier half-lifetime ($\tau_{1/2}$) among the samples. Samples with a larger $\varphi\Sigma\mu_{\text{max}}$ exhibit higher photoconductivity, whereas samples with a longer $\tau_{1/2}$ exhibit slower charge-carrier recombination. TRMC measurements revealed no clear positive correlation between $\varphi\Sigma\mu_{\text{max}}$ and $\tau_{1/2}$ but rather a tendency toward negative correlation. For example, MST-pH10(AA) exhibited the highest $\varphi\Sigma\mu_{\text{max}}$ value ($7.6 \times 10^{-8} \text{ m}^2 \text{ V}^{-1} \text{ s}^{-1}$), indicating efficient carrier generation, whereas its relatively short $\tau_{1/2}$ suggests rapid recombination. By contrast, MST-pH10(FA) exhibited a smaller $\varphi\Sigma\mu_{\text{max}}$ value of $4.1 \times 10^{-8} \text{ m}^2 \text{ V}^{-1} \text{ s}^{-1}$ and a short $\tau_{1/2}$ of 0.29 μs , indicating that both the carrier generation yield and lifetime were limited.

Photocatalytic Activity

The H_2 evolution rates evaluated under visible-light irradiation ($\lambda > 400 \text{ nm}$) are shown in Figure 9. Pt (0.5 wt %) was photodeposited in situ as a cocatalyst in all cases. All of the samples synthesized via the MST method outperformed the SSR-derived sample, with MST-pH10(FA) achieving a H_2 evolution rate of $30 \mu\text{mol h}^{-1}$, approximately 29 times higher than that for the SSR sample. This substantial improvement is attributed primarily to the ~ 85 -fold increase in specific surface area for MST-pH10(FA), which substantially expands the photocatalyst–solution interface. By contrast, MST-pH8(FA), despite having a 1.6-fold higher specific surface area than MST-pH10(FA), exhibited nearly half the photocatalytic activity. The MST-pH10(FA) sample exhibiting the highest activity showed an AQY of 1.8% at 420 nm (Figure S9 in the Supporting Information).

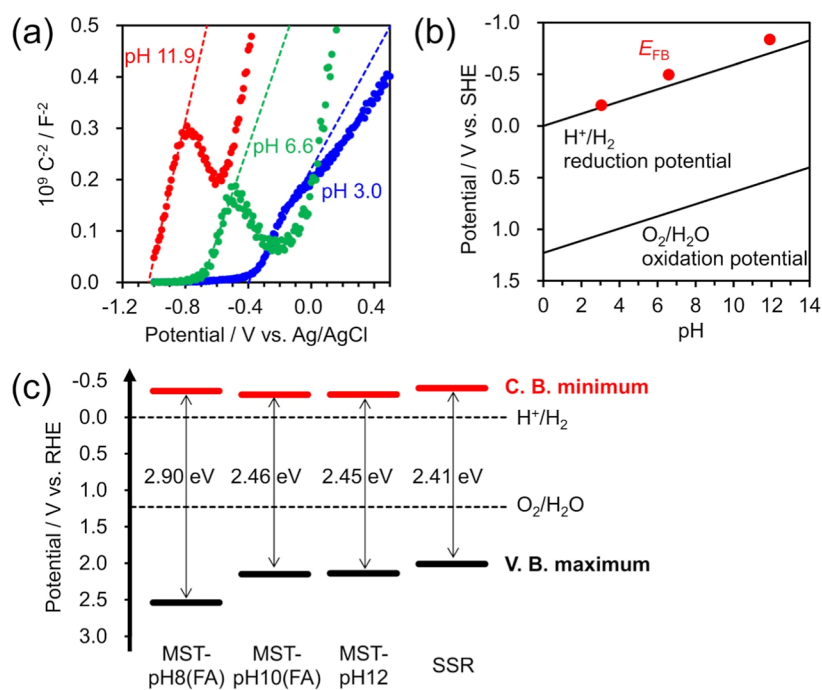


Figure 7. (a) Mott–Schottky plots for MST-pH10(FA) measured under different pH conditions (pH 3.0, 6.6, and 11.9). (b) pH dependence of the flat-band potential (E_{FB}) for MST-pH10(FA), plotted alongside the H^+/H_2 and O_2/H_2O redox potentials versus SHE. (c) Band-edge positions and bandgaps for various PTOF samples (MST-pH8(FA), MST-pH10(FA), MST-pH12, and SSR), showing conduction-band minima and valence-band maxima relative to the reversible hydrogen electrode (RHE).

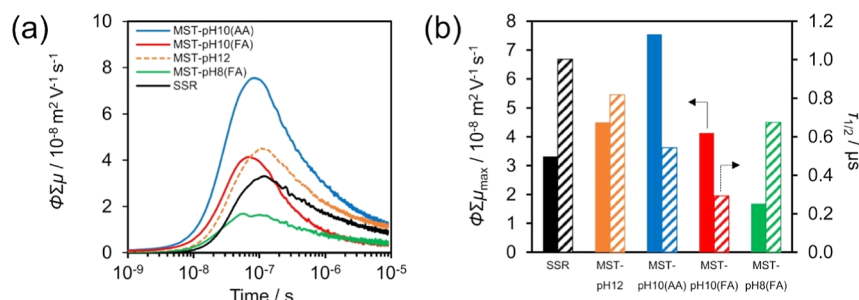


Figure 8. (a) Time-resolved microwave conductivity (TRMC) transient decay for PTOF samples ($\lambda_{ex} = 355$ nm, $I_0 = 9.1 \times 10^{15}$ photons cm^{-2} pulse $^{-1}$). (b) Maximum TRMC signal ($\phi \Sigma \mu_{max}$) and the half-life ($\tau_{1/2}$) for the same samples.

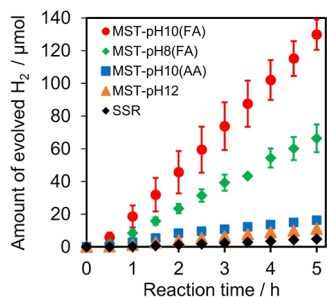


Figure 9. Time courses of H_2 evolution from $Pb_2Ti_2O_{5.4}F_{1.2}$ synthesized by the MST method with different pH adjustments and the SSR method. Reaction conditions: catalyst, 100 mg (Pt 0.5 wt % in situ photodeposited); reaction solution, 10 mM EDTA-2Na (140 mL); light source, 300 W Xe lamp with a CM-1 mirror and a L42 filter ($\lambda > 400$ nm).

XRD and XPS analyses performed before and after the photocatalytic H_2 evolution reaction using the MST-pH10(FA) sample showed no noticeable changes in the crystal

structure, oxidation states of Pb and Ti, or surface composition (Figures S10, S11 and Table S3). These results indicate that the MST-pH10(FA) sample is stable during the H_2 evolution reaction.

Factors Affecting the Photocatalytic Activity

The specific surface area (S_{BET}), bandgap (E_g), $\phi \Sigma \mu_{max}$, and $\tau_{1/2}$ are possible contributors to H_2 evolution activity and are summarized in Table 3. In general, a larger surface area enlarges the photocatalyst–solution interface and increases the number of reactive sites, thereby enhancing photocatalytic activity. However, excessive particle downsizing can lead to reduced crystallinity and increased defect density, which may lower activity, as previously reported.²¹ This trend was also observed in the present study (Figure 10); an obvious trade-off exists between the H_2 evolution activity and S_{BET} .

The carrier supply index ($\phi \Sigma \mu_{max} \times \tau_{1/2}$) integrates the carrier generation efficiency ($\phi \Sigma \mu$) and carrier lifetime ($\tau_{1/2}$), reflecting the overall amount of mobile carriers available for photocatalytic reactions.^{32,33} The carrier supply index sometimes correlates with photocatalytic activity of semiconduc-

Table 3. Physicochemical and Photocatalytic Properties of the PTOF Samples

sample	crystallite size/nm	specific surface area/m ² g ⁻¹	bandgap/eV	$\phi\Sigma\mu_{\max}/\text{m}^2 \text{ V}^{-1} \text{ s}^{-1} \times 10^{-8}$	$\tau_{1/2}/\mu\text{s}$	H ₂ evolution rate/ $\mu\text{mol h}^{-1}$
MST-pH8(FA)	16	60	2.90	1.7	0.68	15
MST-pH10(FA)	28	37	2.46	4.1	0.29	28
MST-pH10(AA)	57	15	2.80	7.6	0.54	3.3
MST-pH12	110	3.9	2.45	4.5	0.82	2.2
SSR	150	0.43	2.41	3.3	1.0	0.96

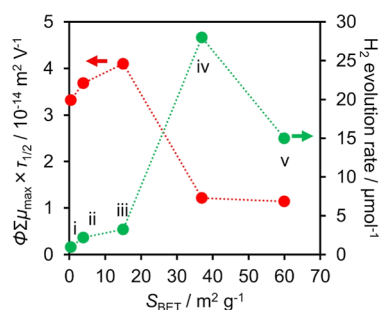


Figure 10. Correlation between $\phi\Sigma\mu_{\max} \times \tau_{1/2}$ and the H₂ evolution rate over PTOF (0.5 wt % Pt in situ photodeposited) with respect to S_{BET} in aqueous EDTA·2Na solution. Data points are labeled as (i) SSR, (ii) MST-pH12, (iii) MST-pH10(AA), (iv) MST-pH10(FA), and (v) MST-pH8(FA).

tors.^{34–36} In the present work, a nearly proportional relationship between $\phi\Sigma\mu_{\max} \times \tau_{1/2}$ and the H₂ evolution rate is found when the S_{BET} values are less than 15 m² g⁻¹ (Figure 10). However, this relationship is not observed for high-activity samples with $S_{\text{BET}} > 40$ m² g⁻¹. Although a larger $\phi\Sigma\mu_{\max} \times \tau_{1/2}$ value generally leads to higher activity, TRMC primarily detects mobile carriers remaining in the bulk. When carriers are rapidly extracted to the surface, $\tau_{1/2}$ and $\phi\Sigma\mu_{\max}$ may appear smaller even under efficient charge separation.³⁷ Therefore, the decrease in $\phi\Sigma\mu_{\max} \times \tau_{1/2}$ observed for high-surface-area samples likely reflects accelerated carrier extraction enabled by the single-crystalline nanoparticle architecture, rather than a loss of carrier generation efficiency. In contrast to previously reported PTOF prepared by SSR or MHT methods,^{20,21,38} where postannealing led to simultaneous increases in both $\phi\Sigma\mu_{\max}$ and $\tau_{1/2}$ as a result of improved crystallinity and reduced defect density, the present MST-derived samples showed an increase only in $\tau_{1/2}$, whereas $\phi\Sigma\mu_{\max}$ remained nearly constant (Figure S12). This result suggests that the photocarrier generation process was already well optimized in the as-synthesized samples and that the enhancement in crystallinity mainly contributed to an extension of the carrier lifetime rather than increasing the carrier generation efficiency. As a result, the H₂ evolution activity changed little after heat treatment (Figure S13), indicating that the photocatalytic performance of the MST samples is governed mainly by carrier extraction rather than by carrier generation.

The BJH pore-distribution analysis revealed that the high-surface-area samples possess mesoporous structures (Figure 3b). As shown in Figure S8, electron microscopy observations revealed that these mesopores do not originate from internal voids within the particles but rather from interparticle spaces formed by the aggregation of single-crystalline nanoparticles, as observed in the MST-pH10(FA) sample. From these structural characteristics, the low-surface-area samples can be regarded as polycrystalline aggregates, whereas the high-surface-area

samples consist of assemblies of single-crystalline nanoparticles. In the latter case, grain-boundary resistance may be negligible, enabling more continuous charge-transport pathways and facilitating the rapid migration of photogenerated carriers to the surface before recombination.³⁹ As a result, even when the $\phi\Sigma\mu_{\max} \times \tau_{1/2}$ value is relatively small, the effective utilization of photogenerated carriers in surface reactions might be possible.

Although MST-pH8(FA), which exhibited the largest surface area (60 m² g⁻¹), showed a carrier supply index similar to that for MST-pH10(FA), the H₂ evolution activity of MST-pH8(FA) was approximately half that of MST-pH10(FA). This difference in activity is likely attributable to an excessive reduction of the particle size, which induces Pb deficiency and bandgap widening, thereby lowering the ability to absorb longer-wavelength light.

CONCLUSIONS

We applied MST synthesis using MEA as the solvent to control the morphology and particle size of the photocatalyst PTOF. Under MST conditions, continuous tuning of the particle size was achieved; at pH 12, micron- to submicron-sized plate-like mesoporous crystals were obtained, whereas at pH 10 (adjusted with formic acid), nanoplatelets with lateral sizes of ~30 nm and thicknesses of several nanometers were formed (MST-pH10(FA)). Crystallographic analysis confirmed the exposure of {112} facets in addition to the dominant {111} facets, although other low- to intermediate-index planes (possibly including {110}) may also be present and could contribute to photocatalytic activity.

Compared with conventional SSR products, the MST-pH10(FA) sample exhibited an approximately 85-fold increase in specific surface area and a 29-fold enhancement in H₂ evolution rate under visible light. In particular, the MST-pH10(FA) sample exhibited the highest photocatalytic activity, which we attributed to the attainment of an appropriate particle morphology within the trade-off between increased specific surface area and bandgap widening.

The results of this work suggest that achieving high photocatalytic performance in the PTOF system requires not an absolute enhancement of carrier generation capacity but rather a well-balanced optimization of the surface reaction environment. In addition, the anisotropic particles obtained in this study provide an important basis and guideline for future investigations aimed at identifying facet-specific oxidation and reduction sites as well as cocatalyst deposition sites.

ASSOCIATED CONTENT

Supporting Information

The Supporting Information is available free of charge at <https://pubs.acs.org/doi/10.1021/acs.chemmater.5c03153>.

XRD patterns obtained under different boric acid ratios, acid washing treatments, and reaction atmospheres

(Figure S1), XRD patterns for PTOF synthesized under pH-adjusted conditions (Figure S2), XPS (Figure S3), Rietveld refinement results of PTOF samples synthesized by different routes (Figure S4), TG-MS (Figure S5), BET surface area versus crystallite size (Figure S6), STEM-EDS images of MST-pH10(FA) with Pt photodeposition (Figure S7), STEM images of MST-pH10(FA) with Pt photodeposition (Figure S8), action spectra and AQY values for H₂ evolution (Figure S9), XRD patterns (Figure S10) and XPS (Figure S11) of MST-pH10(FA) measured before and after the photocatalytic H₂ evolution reaction, TRMC parameters for MST-pH10(FA) after post-treatment (Figure S12), and H₂ evolution activity of MST-pH10(FA) after post-treatment (Figure S13). Data for XRD peak intensities and Lotgering factors (Table S1) and physical properties of PTOF samples (Table S2), surface atomic ratios of MST-pH10(FA) determined by XPS before and after the photocatalytic H₂ evolution reaction (Table S3) (PDF) (PDF)

AUTHOR INFORMATION

Corresponding Author

Kazuhiro Maeda – Department of Chemistry, School of Science, Institute of Science Tokyo, Tokyo 152-8550, Japan; Research Center for Autonomous Systems Materialogy (ASMat), Institute of Science Tokyo, Yokohama, Kanagawa 226-8501, Japan; orcid.org/0000-0001-7245-8318; Email: maeda@chem.sci.isct.ac.jp

Authors

Gentoku Kido – Department of Chemistry, School of Science, Institute of Science Tokyo, Tokyo 152-8550, Japan; Central Research Laboratory, Technology & Development Division, Kanto Chemical Co., Inc., Saitama 340-0003, Japan

Hiroyuki Ueki – Department of Chemistry, School of Science, Institute of Science Tokyo, Tokyo 152-8550, Japan

Megumi Okazaki – Department of Chemistry, School of Science, Institute of Science Tokyo, Tokyo 152-8550, Japan; orcid.org/0000-0003-1167-9453

Jun Kikkawa – Center for Basic Research on Materials, National Institute for Materials Science (NIMS), Tsukuba, Ibaraki 305-0044, Japan; orcid.org/0000-0003-0659-1844

Koji Kimoto – Center for Basic Research on Materials, National Institute for Materials Science (NIMS), Tsukuba, Ibaraki 305-0044, Japan; orcid.org/0000-0002-3927-0492

Ryosuke Nishikubo – Department of Applied Chemistry, Graduate School of Engineering, The University of Osaka, Suita, Osaka 565-0871, Japan; orcid.org/0000-0002-0533-9180

Akinori Saeki – Department of Applied Chemistry, Graduate School of Engineering, The University of Osaka, Suita, Osaka 565-0871, Japan; orcid.org/0000-0001-7429-2200

Complete contact information is available at:

<https://pubs.acs.org/10.1021/acs.chemmater.5c03153>

Author Contributions

The manuscript was written through contributions of all authors. All authors have given approval to the final version of the manuscript.

Notes

The authors declare no competing financial interest.

ACKNOWLEDGMENTS

This research was supported by Grant-in-Aids for Transformative Research Areas (A) “Supra-ceramics” (JP22H05142, JP22H05145, JP22H05148, and JP23H04626) and for Scientific Research (A) (JP25H00899) from the Japan Society for the Promotion of Science (JSPS). We thank Weizhu Zhang of the Center for Basic Research on Materials at the National Institute for Materials Science (NIMS) for preparing the specimens for the STEM measurements. All crystal structure models used in this work were drawn using VESTA.⁴⁰

REFERENCES

- (1) Takata, T.; Jiang, J.; Sakata, Y.; Nakabayashi, M.; Shibata, N.; Nandal, V.; Seki, K.; Hisatomi, T.; Domen, K. Photocatalytic water splitting with a quantum efficiency of almost unity. *Nature* **2020**, *581* (7809), 411–414.
- (2) Iwase, A.; Kato, H.; Kudo, A. A. Simple Preparation Method of Visible-Light-Driven BiVO₄ Photocatalysts From Oxide Starting Materials (Bi₂O₃ and V₂O₅) and Their Photocatalytic Activities. *J. Sol. Energy Eng.* **2010**, *132* (2), 021106.
- (3) Qi, Y.; Zhang, J.; Kong, Y.; Zhao, Y.; Chen, S.; Li, D.; Liu, W.; Chen, Y.; Xie, T.; Cui, J.; et al. Unraveling of cocatalysts photodeposited selectively on facets of BiVO₄ to boost solar water splitting. *Nat. Commun.* **2022**, *13* (1), 484.
- (4) Maeda, K.; Takata, T.; Hara, M.; Saito, N.; Inoue, Y.; Kobayashi, H.; Domen, K. GaN:ZnO solid solution as a photocatalyst for visible-light-driven overall water splitting. *J. Am. Chem. Soc.* **2005**, *127* (23), 8286–8287.
- (5) Maeda, K.; Teramura, K.; Lu, D.; Takata, T.; Saito, N.; Inoue, Y.; Domen, K. Photocatalyst releasing hydrogen from water. *Nature* **2006**, *440* (7082), 295.
- (6) Maeda, K.; Domen, K. Photocatalytic Water Splitting: Recent Progress and Future Challenges. *J. Phys. Chem. Lett.* **2010**, *1* (18), 2655–2661.
- (7) Kageyama, H.; Hayashi, K.; Maeda, K.; Attfield, J. P.; Hiroi, Z.; Rondinelli, J. M.; Poeppelmeier, K. R. Expanding frontiers in materials chemistry and physics with multiple anions. *Nat. Commun.* **2018**, *9* (1), 772.
- (8) Scaife, D. E. Oxide semiconductors in photoelectrochemical conversion of solar energy. *Sol. Energy* **1980**, *25* (1), 41–54.
- (9) Peng, Y.; Wang, D.; Zhou, H.-Y.; Xu, A.-W. Controlled synthesis of thin BiOCl nanosheets with exposed {001} facets and enhanced photocatalytic activities. *CrystEngComm* **2015**, *17* (20), 3845–3851.
- (10) Zhang, J.; Liu, K.; Zhang, B.; Zhang, J.; Liu, M.; Xu, Y.; Shi, K.; Wang, H.; Zhang, Z.; Zhou, P.; et al. Anisotropic Charge Migration on Perovskite Oxy sulfide for Boosting Photocatalytic Overall Water Splitting. *J. Am. Chem. Soc.* **2024**, *146* (6), 4068–4077.
- (11) Lin, L.; Nakabayashi, M.; Lu, D.; Hisatomi, T.; Takata, T.; Domen, K. Formation Mechanism for Particulate Y₂Ti₂O₅S₂ Photocatalyst by the Solid-State Reaction. *Chem. Mater.* **2024**, *36* (3), 1612–1620.
- (12) Chen, K.; Xiao, J.; Vequizo, J. J. M.; Hisatomi, T.; Ma, Y.; Nakabayashi, M.; Takata, T.; Yamakata, A.; Shibata, N.; Domen, K. Overall Water Splitting by a SrTaO₂N-Based Photocatalyst Decorated with an Ir-Promoted Ru-Based Cocatalyst. *J. Am. Chem. Soc.* **2023**, *145* (7), 3839–3843.
- (13) Masubuchi, Y.; Koyama, K.; Hosono, A.; Higuchi, M.; Takesada, M.; Shitara, K.; Moriwake, H.; Kikkawa, S. Average Cubic BaTaO₂N Crystal Structure Formed by 50 nm Size Domains with Polar Nanoregions Consisting of cis-TaO₄N₂ Octahedral Chains. *Chem. Mater.* **2024**, *36* (15), 7504–7513.
- (14) Hojamberdiev, M.; Yubuta, K.; Vequizo, J. J. M.; Yamakata, A.; Oishi, S.; Domen, K.; Teshima, K. NH₃-Assisted Flux Growth of Cube-like BaTaO₂N Submicron Crystals in a Completely Ionized

Nonaqueous High-Temperature Solution and Their Water Splitting Activity. *Cryst. Growth Des.* **2015**, *15* (9), 4663–4671.

(15) Hsieh, P.-L.; Naresh, G.; Huang, Y.-S.; Tsao, C.-W.; Hsu, Y.-J.; Chen, L.-J.; Huang, M. H. Shape-Tunable SrTiO₃ Crystals Revealing Facet-Dependent Optical and Photocatalytic Properties. *J. Phys. Chem. C* **2019**, *123* (22), 13664–13671.

(16) Kuriki, R.; Ichibha, T.; Hongo, K.; Lu, D.; Maezono, R.; Kageyama, H.; Ishitani, O.; Oka, K.; Maeda, K. A Stable, Narrow-Gap Oxyfluoride Photocatalyst for Visible-Light Hydrogen Evolution and Carbon Dioxide Reduction. *J. Am. Chem. Soc.* **2018**, *140* (21), 6648–6655.

(17) Walsh, A.; Payne, D. J.; Egdell, R. G.; Watson, G. W. Stereochemistry of post-transition metal oxides: revision of the classical lone pair model. *Chem. Soc. Rev.* **2011**, *40* (9), 4455–4463.

(18) Oka, K.; Hojo, H.; Azuma, M.; Oh-ishi, K. Temperature-Independent, Large Dielectric Constant Induced by Vacancy and Partial Anion Order in the Oxyfluoride Pyrochlore Pb₂Ti₂O_{6-δ}F_{2δ}. *Chem. Mater.* **2016**, *28* (15), 5554–5559.

(19) Mizuochi, R.; Hirayama, N.; Maeda, K. Photoelectrochemical Water Oxidation over Pb₂Ti₂O_{5.4}F_{1.2} Photoanodes Prepared by the Particle Transfer Method. *J. Phys. Chem. C* **2023**, *127* (44), 21544–21551.

(20) Aihara, K.; Mizuochi, R.; Okazaki, M.; Nishioka, S.; Yasuda, S.; Yokoi, T.; Ishiwari, F.; Saeki, A.; Inada, M.; Maeda, K. Low-Temperature Microwave-Assisted Hydrothermal Synthesis of Pb₂Ti₂O_{5.4}F_{1.2} Photocatalyst for Improved H₂ Evolution under Visible Light. *ACS Mater. Lett.* **2023**, *5* (9), 2355–2360.

(21) Ueki, H.; Tanaka, T.; Anabuki, S.; Nakada, R.; Okazaki, M.; Aihara, K.; Hattori, M.; Ishiwari, F.; Haruki, R.; Nozawa, S.; et al. Mesoporous Oxyhalide Aggregates Exhibiting Improved Photocatalytic Activity for Visible-Light H₂ Evolution and CO₂ Reduction. *ACS Catal.* **2025**, *15* (14), 12551–12562.

(22) Boochakiat, S.; Tantraviwat, D.; Thongsook, O.; Pornsuwan, S.; Nattestad, A.; Chen, J.; Channei, D.; Inceesungvorn, B. Effect of exposed facets of bismuth vanadate, controlled by ethanolamine, on oxidative coupling of primary amines. *J. Colloid Interface Sci.* **2021**, *602* (15), 168–176.

(23) Liu, T.; Geng, X.; Mu, Y.; Fan, C.; Huang, S. Hierarchical TaO₂F microspheres assembled by nanosheets and their application in infrared and microwave transparency and lithium-ion batteries. *Vacuum* **2025**, *239*, 114367.

(24) Zhou, L.; Smyth Boyle, D.; O'Brien, P. Uniform NH₄TiOF₃ mesocrystals prepared by an ambient temperature self-assembly process and their topotaxial conversion to anatase. *Chem. Commun.* **2007**, 144–146.

(25) Scherrer, P. Bestimmung der inneren Struktur und der Größe von Kolloidteilchen mittels Röntgenstrahlen. *Nachr. Ges. Wiss. Göttingen, Math.-Phys. Kl.* **1918**, 98–100.

(26) Lotgering, F. K. *Topotactical Reactions with Ferrimagnetic Oxides Having Hexagonal Crystal Structures-i*; Pergamon Press Ltd, 1959.

(27) Rodríguez-Carvajal, J. Recent advances in magnetic structure determination by neutron powder diffraction. *Phys. B* **1993**, *192* (1–2), 55–69.

(28) Izumi, F.; Momma, K. Three-Dimensional Visualization in Powder Diffraction. *Solid State Phenom.* **2007**, *130* (1662–9779), 15–20.

(29) Maeda, K.; Eguchi, M.; Lee, S. H. A.; Youngblood, W. J.; Hata, H.; Mallouk, T. E. Photocatalytic hydrogen evolution from Hexaniobate nanoscrolls and calcium niobate nanosheets sensitized by ruthenium(II) bipyridyl complexes. *J. Phys. Chem. C* **2009**, *113* (18), 7962–7969.

(30) Rouquerol, F.; Rouquerol, J.; Sing, K. S. W. *Adsorption by Powders and Porous Solids: Principles, Methodology and Applications*; Academic Press, 1999.

(31) Bensaid, S.; Piumetti, M.; Novara, C.; Giorgis, F.; Chiodoni, A.; Russo, N.; Fino, D. Catalytic Oxidation of CO and Soot over Ce-Zr-Pr Mixed Oxides Synthesized in a Multi-Inlet Vortex Reactor: Effect of Structural Defects on the Catalytic Activity. *Nanoscale Res. Lett.* **2016**, *11* (1), 494.

(32) Saeki, A.; Koizumi, Y.; Aida, T.; Seki, S. Comprehensive approach to intrinsic charge carrier mobility in conjugated organic molecules, macromolecules, and supramolecular architectures. *Acc. Chem. Res.* **2012**, *45* (8), 1193–1202.

(33) Saeki, A.; Yoshikawa, S.; Tsuji, M.; Koizumi, Y.; Ide, M.; Vijayakumar, C.; Seki, S. A versatile approach to organic photovoltaics evaluation using white light pulse and microwave conductivity. *J. Am. Chem. Soc.* **2012**, *134* (46), 19035–19042.

(34) Suzuki, H.; Higashi, M.; Kunioku, H.; Abe, R.; Saeki, A. Photoconductivity–Lifetime Product Correlates Well with the Photocatalytic Activity of Oxyhalides Bi₄TaO₈Cl and PbBiO₂Cl: An Approach to Boost Their O₂ Evolution Rates. *ACS Energy Lett.* **2019**, *4* (7), 1572–1578.

(35) Suzuki, H.; Kanno, S.; Hada, M.; Abe, R.; Saeki, A. Exploring the Relationship between Effective Mass, Transient Photoconductivity, and Photocatalytic Activity of Sr_xPb_{1-x}BiO₂Cl (*x* = 0–1) Oxyhalides. *Chem. Mater.* **2020**, *32* (10), 4166–4173.

(36) Saeki, A. Evaluation-oriented exploration of photo energy conversion systems: from fundamental optoelectronics and material screening to the combination with data science. *Polym. J.* **2020**, *52* (12), 1307–1321.

(37) Tamura, Y.; Okazaki, M.; Ueki, H.; Aihara, K.; Kanazawa, T.; Fan, D.; Haruki, R.; Iwase, A.; Nozawa, S.; Ishiwari, F.; et al. Modification of Visible-Light-Responsive Pb₂Ti₂O_{5.4}F_{1.2} with Metal Oxide Cocatalysts to Improve Photocatalytic O₂ Evolution toward Z-Scheme Overall Water Splitting. *ChemSusChem* **2024**, *17* (12), No. e202400408.

(38) Wakayama, H.; Kato, K.; Kashiara, K.; Uchiyama, T.; Miyoshi, A.; Nakata, H.; Lu, D.; Oka, K.; Yamakata, A.; Uchimoto, Y.; et al. Activation of a Pt-loaded Pb₂Ti₂O_{5.4}F_{1.2} photocatalyst by alkaline chloride treatment for improved H₂ evolution under visible light. *J. Mater. Chem. A* **2020**, *8* (18), 9099–9108.

(39) Lakshminarasimhan, N.; Kim, W.; Choi, W. Effect of the Agglomerated State on the Photocatalytic Hydrogen Production with in Situ Agglomeration of Colloidal TiO₂ Nanoparticles. *J. Phys. Chem. C* **2008**, *112* (51), 20451–20457.

(40) Momma, K.; Izumi, F. VESTA 3 for three-dimensional visualization of crystal, volumetric and morphology data. *J. Appl. Crystallogr.* **2011**, *44* (6), 1272–1276.